# Facile Preparation of Hierarchical TiO₂ Nanowire-Nanoparticle/Nanotube Architecture for Highly Efficient Dye-Sensitized Solar Cells

Nianqing Fu [a,b,c], Yan Liu [c], Wei Lu [c], Feng Peng [a], Limin Zhou [d], Yanchun Liu [b]*, Haitao Huang [c]*


[a]School of Chemistry and Chemical Engineering, South China University of Technology, Guangzhou 510640, China.

[b]The Key Laboratory of Energy-Efficient Functional Ceramics and Applied Technology of Guangdong Province, Guangzhou Redsun Gas Applications Co., LTD, Guangzhou, 510435, China.

[c]Department of Applied Physics, The Hong Kong Polytechnic University, Hung Hom, Kowloon, Hong Kong, China.

[d]Department of Mechanical Engineering, The Hong Kong Polytechnic University, Hong Kong, China.


Corresponding author information:

E-mail address: aphhuang@polyu.edu.hk (H. Huang), Tel: +852-2766-5694; Fax: +852-2333-7629

E-mail address: lyc21@163.com (Y. Liu), Tel: 020-36372332, Fax: 020-22855228

**Table of contents entry:**

Hierarchical TiO$_2$ architecture with remarkably improved surface area and light scattering effect was prepared via one-step post-treatment for dye-sensitized solar cells, achieving a high efficiency of 8.82%.

**TOC image**
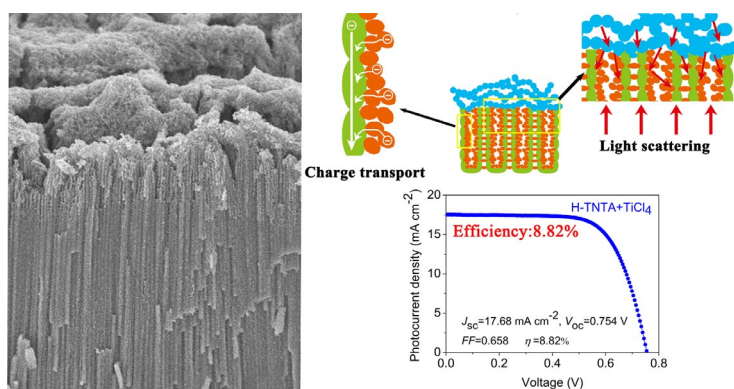
**Abstract**

In the present work, we developed a facial and chemical-free post-treatment approach, namely one-step hot-water soaking, to the fabrication of double-layer and hierarchical $TiO_2$ nanotube arrays (H-TNTA) comprising of a nanoparticle/nanotube hybrid layer and a $TiO_2$ nanowire cap layer for highly efficient dye-sensitized solar cells (DSSCs). The nanoparticle/nanotube hybrid structure of the H-TNTA provides enormous specific surface area for sufficient dye attachment and the $TiO_2$ nanowire cap layer serves as a light-scattering layer with increased dye-absorbing for superior light harvesting efficiency. This engineered integration makes it possible to control the dye-anchoring, charge transport, charge collection, and light scattering within a photoanode simultaneously. The DSSC based on the well tailored architecture yields an exciting power conversion efficiency of 8.21% under 100 mW $cm^{-2}$, corresponding to 51% improvement as compared with the cell built on the pristine TNTA (P-TNTA, 5.43%). The efficiency can be further improved to 8.82% when the H-TNTA photoanodes are subjected to an additional $TiCl_4$ treatment.


**Keyword**: dye-sensitized solar cell, hierarchical structure, light-scattering, cap layer, post-treatment

**Introduction**

Among the various photovoltaic devices, dye-sensitized solar cells (DSSCs) have attracted much interest due to their simple fabricating process, low cost and high power conversion efficiency.[1-9] As one of the most important components of DSSCs, the photoanode, with a sensitized semiconductor thin film, plays a key role in dye loading, electron injection, charge transport and charge collection.[8-15] In a conventional DSSC, a ~10 μm thin film comprising of randomly dispersed nanoparticles, which are of high specific surface area for efficient dye loading, is typically employed as the photoanode.[2,15] However, the disordered network in the film also creates numerous grain boundaries, surface defects and traps states, which slow the electron transport and increase the charge recombination, limiting the further improvement in charge collection efficiency and device performance.[8-12,16-19] Hence, improving the charge transport is highly demanding and deemed effective to improve the cell efficiency.[8-10,13-14] Several one-dimensional (1D) nanostructures, such as nanorods,[20,21] nanowires,[10,22-24] and nanotubes,[7-9,25-27] have been exploited as photoanodes to overcome the shortcoming of charge transport in DSSCs, owing to their vectorial pathway for fast electron transport along the axial direction. In particular, extensive attention has been paid to $TiO_2$ nanotube array (TNTA) because of its high self-organization, simple fabrication process, controllable geometry, and good light-trapping property.[7-9,25-27] However, the pristine TNTA (P-TNTA) with smooth walls usually possesses a low specific surface area that is only 1/2 or 1/3 that of the nanoparticle-based $TiO_2$ films.[7,8,28] The low specific surface area of P-TNTA is one of the major factors responsible for the low device efficiency, due to the low dye-loading capacity and the resulted inadequate light harvesting.[7-10]

In the past few years, considerable efforts have been made to increase the surface area of the anodized P-TNTA for enhanced DSSC efficiency, which include (a) tuning of the TNTA morphology by adjusting the anodization parameters and (b) decorating the TNTA wall with nanoparticles *via* a post-treatment to form a hierarchical structure.[7-9, 29-35] By changing the anodization parameters, TNTAs with tunable tube diameter,[29,30] varying wall thickness and shape,[8,31] and photonic crystal geometry[25,26,32] have been fabricated and applied in DSSCs with enhanced performance. However, these techniques do not significantly increase the surface area and the DSSC efficiency is still not encouraging enough. By filling small nanoparticles into the nanotubes, Pan *et al*. doubled the efficiency of the TNTA based DSSCs.[35] The soaking of amorphous TNTA in DI water or $NH_4F$ aqueous solution leads to a coarse nanotube surface, which improves the cell efficiency to a certain degree.[33,34] Among the various techniques, $TiCl_4$ treatment demonstrates itself the most effective technique to increase the surface area and suppress electron recombination, which can promote the device efficiency remarkably.[7-9] Recently, Park *et al*. reported a record efficiency up to 11.3% by employing a $TiCl_4$ treated TNTA photoanode.[9]

Even though the TNTA has an intrinsic light scattering effect, its ordered nano-porous structure still leads to a loss of incident light at the wavelength ~ 600-800 nm.[36] Meanwhile, the commonly used dye (such as N719 and N3) also exhibits a low molar extinction coefficient in this long wavelength range. Therefore, increasing the light travelling path in the 1D structured film by using a light-scattering layer is another approach to enhanced cell efficiency, apart from increasing the surface area.[30,37] Microspheres, nanotubes and nanofibers are commonly used in the scattering layer which is normally deposited on the $TiO_2$

nanoparticle absorption layer by a lay-by-layer technique to form the photoanodes of DSSCs.[30,36-39] However, the multilayer structure derived from this stamping technique also increases the charge transport resistance, especially at the interface between different layers.[37] *In-situ* growth of the scattering layer directly on the $TiO_2$ absorption layer seems to be a promising solution to this problem.[6]

Herein, we report a facial and chemical-free post treatment to fabricate *in-situ* a $TiO_2$ fiber-nanoparticle/nanotube hierarchically structured photoanode for high efficiency DSSC. In this one-step treatment, nanoparticle/nanotube hierarchical structure together with a $TiO_2$ nanowire light-scattering cap layer can be achieved simultaneously. This well-designed structure enables the photoanode a high specific surface area for sufficient dye loading and a superior scattering effect for adequate light harvesting. Meanwhile, it also retains the excellent 1D electron-transport feature in the film for fast charge collection. The DSSC employing this well-tailored photoanode achieved a high efficiency up to 8.21%, which can be further improved to 8.82% when the photoanode was subjected to an additional $TiCl_4$ treatment.

**Experimental**

**2.1 Preparation of TNTA by anodization**

Highly ordered P-TNTAs were prepared by a two-step electrochemical anodization technique, using a two-electrode electrochemical cell with Ti foil as the anode and Pt foil as the cathode. Prior to anodization, the Ti foil (0.125 mm thick, 99.7% purity, Strem Chemicals) was cleaned in detergent, acetone, ethanol and distilled water (DI water) successively. The Ti foil was then anodized at 60V in ethylene glycol (EG) electrolyte containing 0.5 wt% $NH_4F$

and 3 % (in volume) DI water for 1.5 h. The formed anodic $TiO_2$ layer was peeled off by ultrasonication in a water bath. The treated Ti foil with fresh surface was subjected to a second anodization under the same condition for 2h. Then as-prepared TNTA was dipped into ethanol to remove the electrolyte and annealed at 450°C for 2h. Free-standing TNTA membrane was obtained by subjecting the annealed Ti foil to a third-anodization for around 2h. Highly crystallized anatase pristine TNTA (P-TNTA) was obtained by annealing the free-standing membrane at 500°C for 2h.

## 2.2 Fabrication of hierarchical TNTA by post treatment

To fabricate hierarchical TNTA (H-TNTA) membranes, the as-anodized electrodes after the second anodization were soaked in ethanol first and then immerged in hot DI water at 60°C for 24 h. The hot DI water-soaking post treatment process was conducted in a fume hood. After cooling down, the electrodes were dipped into $H_2O_2$ for 10 s and then rinsed by ethanol and DI water alternatively. By slightly bending the electrodes, the H-TNTA membranes were self-detached from the Ti foils during the drying process. The obtained H-TNTA membranes were sintered at 500°C for 2h.

## 2.3 Fabrication of DSSCs

The free-standing P-TNTA and H-TNTA membranes were attached to the well-cleaned fluorine-doped tin oxide (FTO) glass substrates to form the photoanodes, using a ~2 μm thick $TiO_2$ nanoparticle (hydrothermally prepared, ~14 nm in diameter) layer as the adhesive layer. They were annealed at 500°C for 2h and then sensitized in an N719 ethanol solution (0.3 mM, Solaronix, Switzerland) at room temperature for 36 h. The platinized counter electrodes were prepared by thermal decomposition of 5 mM $H_2PtCl_6$/isopropanol solution on FTO glass at

390°C for 15 min. The sensitized photoanodes and counter electrodes were sandwiched to form DSSCs, using 25 μm Surlyn 1702 films as spacer. The liquid electrolyte composing of 0.5 M LiI, 0.05 M $I_2$, 0.3 M 1-methyl-3-hexylimidazolium iodide (HMII), 0.3 M *N*-methylbenzimidazole (NMB), and 0.5 M 4-*tert*-butylpyridine in 3-methoxypropionitrile was filled between the two electrodes. The active area of the DSSCs is 0.16 cm$^2$.

## 2.4   Measurements and Characterizations

The structure and morphology of the TNTA were observed by field-emission scanning electron microscope (FESEM, FEI Sirion 200) and transmission electron microscope (TEM, JEOL JEM-2100F). X-ray diffraction (XRD, Rigaku 9KW SmartLab, Japan) patterns were recorded for crystal phase identification. The optical properties of the TNTA photoanodes and the dye-loading amounts were measured by an UV-vis spectrophotometer (Model UV-2550, Shimadzu, Japan). The surface area was evaluated using a Quantachrome NOVA 2000e analyzer. The Brunauer−Emmett−Teller (BET) and Barrent-Joyner-Halenda (BJH) methods were used to estimate the specific surface area (SSA). *I–V* characteristics were tested using a Keithley 2420 source meter under AM 1.5 G illumination (100 mW cm$^{-2}$) supplied by a 300 W solar simulator (Model 69911, Newport-Oriel Instruments, USA). The input illumination was calibrated using a silicon reference cell (NIST) equipped with a power meter. The IPCE measurements were conducted on a Newport 2931-C power meter combined with a Newport 74125 monochromator. The light source was provided by a Newport 66902 solar simulator. The electrochemical impedance spectra (EIS) were collected under 100 mW cm$^{-2}$ illumination, using a CHI instrument (CHI 660C, CH Instruments, USA) at the open circuit voltage with an ac perturbation signal of amplitude 10 mV in a frequency range from $10^5$ to $10^{-2}$ Hz. The

intensity-modulated photocurrent spectroscopy (IMPS) and intensity-modulated photovoltage spectroscopy (IMVS) measurements were performed on the same sandwiched cells, using a high power green light emitting diode (LED, peak wavelength 520 nm). The LED provides both *dc* and *ac* components of the illumination. The light intensity was modulated (±8%) by modulating the voltage applied to the LED. The light intensity on the tested cells was calibrated by a Si cell.

**Result and discussion**

Fig. 1 schematically illustrates the simple procedure to fabricate the hierarchical H-TNTA architecture with the merits of (a) vectorial pathway for fast oriented electron transport, (b) coarse surface for large dye absorbing capacity, (c) excellent light-scattering effect favoring efficient light harvesting. Two key steps involved in the fabrication process are the preparation of amorphous TNTA by electrochemical anodization and the post-treatment of the TNTA in hot water of 60°C.

Fig. 2 (a) and (b) show the typical morphologies of the P-TNTA obtained after the second anodization process, with a smooth tube wall and a thin top layer left by the first anodization. It is reported that the as-prepared TNTA are amorphous with a double walled structure, outer and inner walls.[8] The comparable thicker inner wall usually contains a large amount of impurities, such as $[TiF_6]^{2-}$ compounds.[8,40] The amorphous $TiO_2$ is inclined to be dissolved into various solvents, such as DI water.[33,34,40] In this study, it was assumed that, during the hot water soaking treatment, the amorphous $TiO_2$, especially the inner wall of nanotubes containing $[TiF_6]^{2-}$ compound, will be dissolved into the hot water according to Equations 1 and 2. In this process, the dissolved $F^-$ anions in the solution may also accelerate
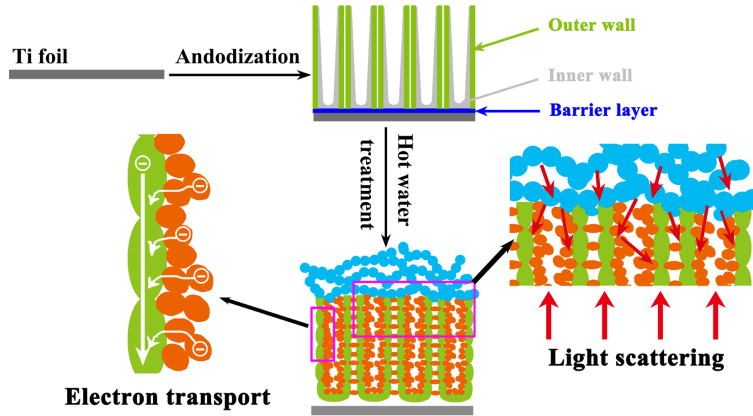
**Fig. 1** Schematic illustration of the procedure to fabricate the hierarchical H-TNTA architecture with the designed merits.

the dissolution of the amorphous $TiO_2$, according to Equations 2 and 3. Meanwhile, the $Ti^{4+}$ cations in the solution may also react with $H_2O$ (Equation 4) and redeposit on the wall surface to form $TiO_2/Ti(OH)_4$ nanoparticles.[40] During the following annealing process, these titanium compounds will be crystallized into $TiO_2$ nanoparticles and attached tightly onto the tube wall surface to form a $TiO_2$ nanopartilce/nanotube array hybrid structure, as shown in Fig. 2 (c), (f) and (g). Since the whole post treatment process was conducted in a fume hood, the air agitation accelerated the evaporation of the hot water (~ 3/5 of the water was evaporated within 24 h). The loss of a large proportion of water increased the $Ti^{4+}$ concentration in the remaining solution and accelerated the deposition of $TiO_2$ (Equation 4) on the top surface of the TNTA. As a result, a cap layer (~ 2 μm in thickness) composing of $TiO_2$ nanowires

$$TiO_2 + 2H_2O \rightarrow Ti^{4+} + 4OH^- \tag{1}$$

$$[TiF_6]^{2-} \xrightarrow{H_2O} Ti^{4+} + 6F^- \tag{2}$$

$$TiO_2 + 6F^- \xrightarrow{4H^+} [TiF_6]^{2-} + 2H_2O \tag{3}$$

$$Ti^{4+} + 2H_2O \rightarrow TiO_2 + 4H^+ \tag{4}$$

(~ 100 nm in diameter and several microns in length) are formed on the top of TNTA which forms an ideal hierarchical H-TNTA structure, as shown in Fig. 2 (c)-(e).
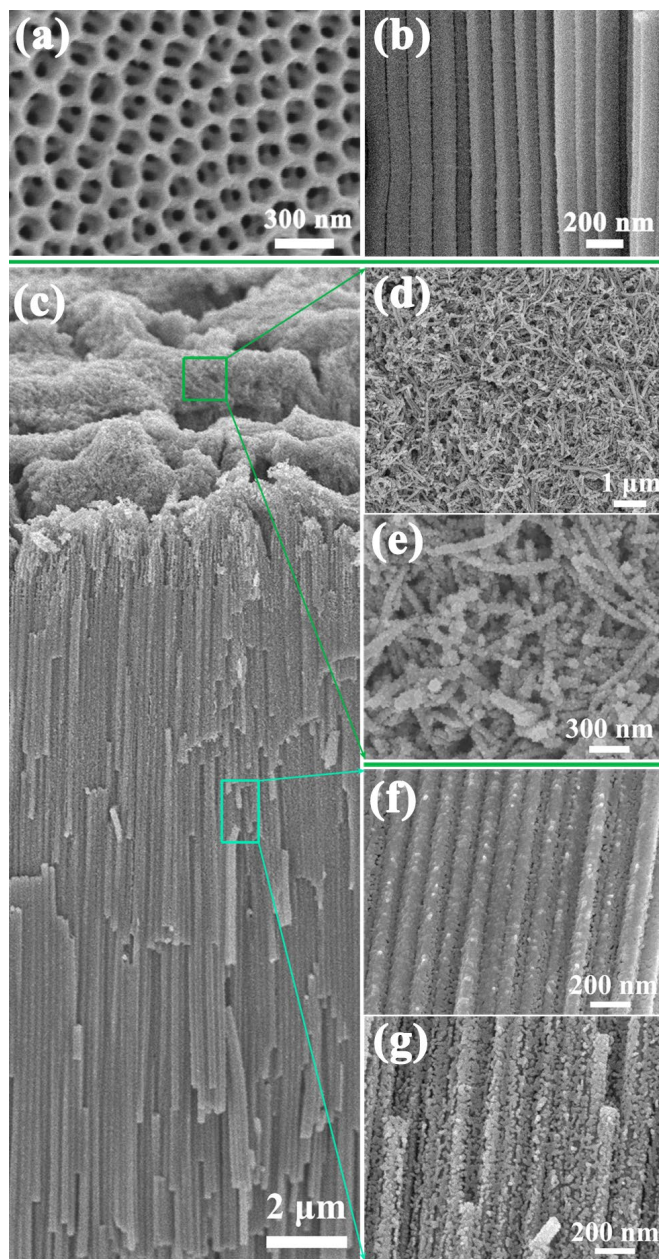


**Fig. 2** SEM images of the (a) top and (b) cross-section of the pristine TNTA; (c) cross-section of the TNTA after hot water post-treatment (H-TNTA); (d, e) top-views of the nanowire based cap layer of H-TNTA; and the cross-section views of the (f) outer wall and (g) inner wall of the H-TNTA.

As displayed in the TEM images of Figs. 3 (a) and (b), the P-TNTA demonstrates a smooth tube wall with a wall thickness around 29 nm. This smooth 1D structure often possesses insufficient surface area for dye attachment. Moreover, some impurity phase can be observed clearly in the TEM images, as marked in Fig. 3a. These impurities many be $TiF_x$ or $TiC_x$ compounds and will act as trap-sites for electron recombination in a DSSC, declining the device performance.[8,40] In contrast, as revealed in Figs. 3 (c) and (d), coarse tube walls were formed in H-TNTA after the hot water treatment of P-TNTA for 24 h, with lots of small particles decorated on both the inner and outer surfaces of the tube wall. It is worth noting that, the tube walls were composed of columnar crystals connecting to each other, oriented along the tube axial direction. A comparison of Figs. 3 (b) and (d) demonstrates that the wall thickness of H-TNTA was shrunk from 29 nm (for P-TNTA) to 20 nm because part of the amorphous tube wall was dissolved and converted into $TiO_2$ nanoparticles to form the H-TNTA hybrid structure. Noticeably, the impurities observed in P-TNTA were disappeared in H-TNTA sample, after the post-treatment. The nanoparticle/nanotube hybrid structure in H-TNTA is in favor of (i) large dye loading amount due to its rough wall surface decorated with the $TiO_2$ nanoparticles and (ii) fast electron transport and efficient charge collection due to the oriented packing of the columnar nanocrystals. Figs. 3 (e) and (f) clearly demonstrate that the $TiO_2$ nanowires in the cap layer of H-TNTA are aggregates of small nanoparticles (~ 15-40 nm in size). This cap layer can act as not only a scattering layer, but also a dye-anchoring layer, both in favor of light harvesting. Anatase $TiO_2$ was confirmed in both P-TNTA and H-TNTA, as judged from the $d_{(101)}$-spacing of 0.352 nm (Figs. 3(b), (d) and (f)).
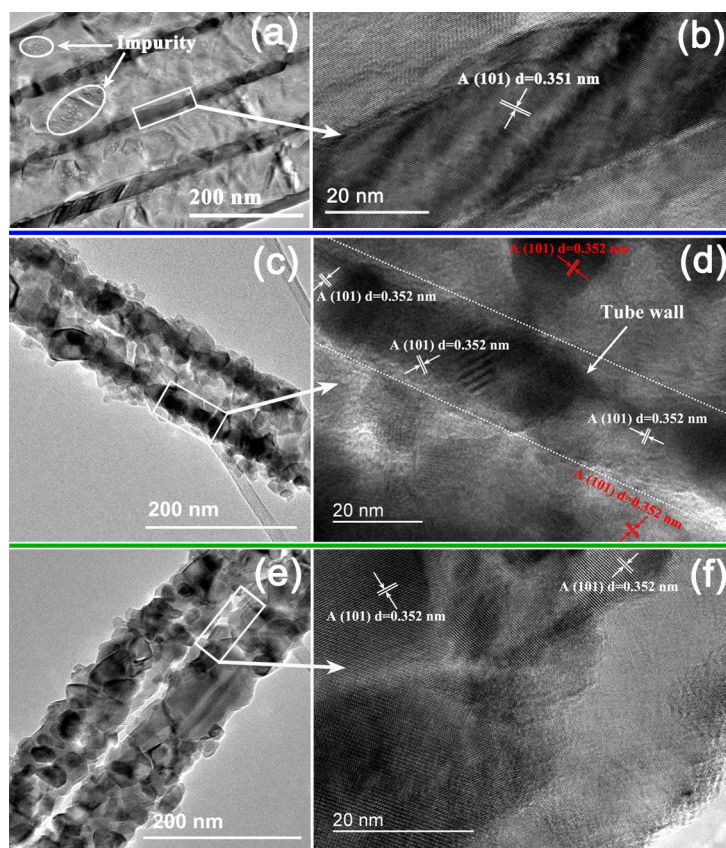
**Fig. 3** Low magnification (a) and high magnification (b) TEM images of P-TNTA; (c) and (d) TEM images of H-TNTA with low and high magnification; (e) and (f) TiO$_2$ nanowire in the cap layer of H-NTNA.

XRD measurements revealed that all the TiO$_2$ samples were crystallized after the annealing at 500°C in air for 2h. As shown in Fig. 4, the emergence of (101), (004), (200), and (105) peaks centering at 25.24°, 37.75°, 47.98°, and 53.78°, respectively, suggests the formation of anatase TiO$_2$. No impurity phase can be detected from the XRD pattern for both samples, since the small amount of impurities observed in P-TNTA by TEM (Fig. 3b) is below the detection limit of XRD. A detailed comparison of the XRD patterns of the P-TNTA and H-TNTA samples shows that the full width at half maximum (FWHM) of almost all the diffraction peaks of H-TNTA is broadened (inset of Fig. 4), indicating a reduced grain size. The average gain size was calculated to be 28.3 and 19.4 nm for P-TNTA and H-TNTA,

respectively. The decreased grain size of H-TNTA can be attributed to the dissolution of $TiO_2$ during hot water treatment (Equations 1 and 3), leading to significantly increased specific surface area for considerable improvement in dye loading. The $N_2$ adsorption-desorption isotherms reveal that the BET surface area of the H-TNTA membrane is increased remarkably to 46.8 $m^2$ $g^{-1}$ which almost doubles that of the P-TNTA film (Table 1).
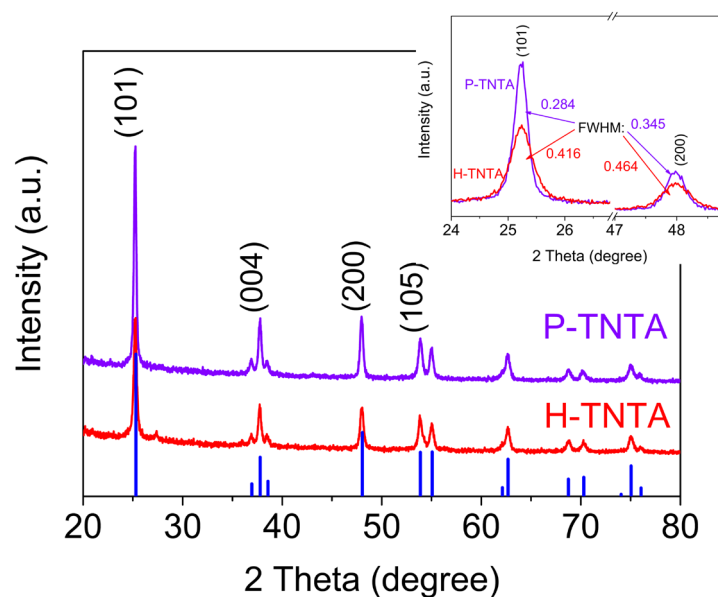


**Fig. 4** XRD patterns of H-TNTA and P-TNTA. The inset compares the full width at half maximum (FWHM) of the (101) and (200) diffraction peaks of the two samples.

To determine the amount of dye loading, the sensitized electrodes (with an active area of 1.5 $cm^2$) were immersed in 0.1 M NaOH aqueous solution and the desorbed dye solutions were measured by UV-Vis spectroscopy. The dye loading amount was calculated to be $2.19 \times 10^{-7}$ mol $cm^{-2}$ for H-TNTA, about twice that of the P-TNTA electrode ($1.02 \times 10^{-7}$ mol $cm^{-2}$), as evidenced from the absorbance spectra of the detached dye solutions (Fig. 5a). Both the increased dye loading and the scattering cap layer of the H-TNTA sample will contribute to the light harvesting and hence the device performance.
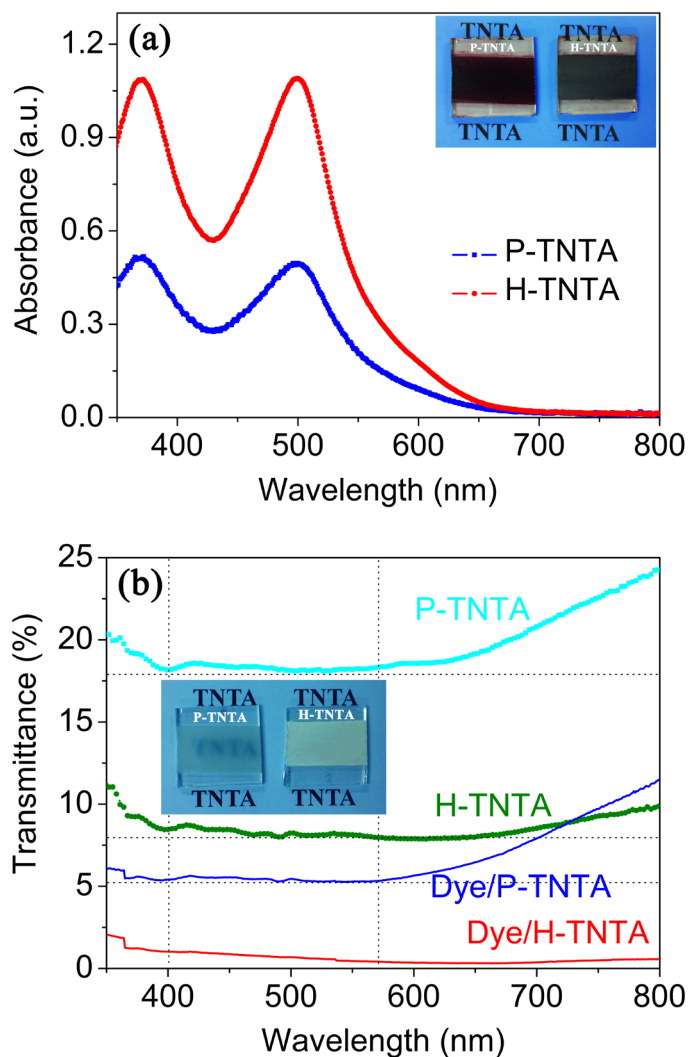
**Fig. 5** (a) UV-Vis absorbance spectra of the solutions containing dyes detached from the sensitized P-TNTA and H-TNTA electrodes. The inset shows the P-TNTA and H-TNTA electrodes sensitized with the N719 dye; (b) UV-Vis transmittance spectra of the P-TNTA and H-TNTA electrodes before and after N719 sensitizing. The inset is the electrodes before sensitizing, showing the transparency of the films.

It is well known that many organic dyes, such as N3 and N719, commonly used in DSSCs exhibit a wavelength dependent light absorption, with quite a high molar extinction coefficient within a wavelength of 450-550 nm, which quickly decreases in a range large than 600 nm.[41] Usually, the incident light (1 Sun) at 540 nm can be absorbed completely by a N719 sensitized film with a thickness of a few micrometers, whereas an absorption distance up to

tens of millimeters is required to fully utilize the input light at 700 nm.[41] In this regard, prolonging the optical path length in photoanode, which can be realized by photon trapping or scattering, is another route to improve the light harvesting efficiency and upgrade the performance of DSSCs. As shown in Fig. 5b and its inset, the P-TNTA sample is semitransparent with a transmittance around 18% in the wavelength range of 400-600 nm. However, the transmittance rises remarkably when the wavelength is larger than 600 nm, owing to the easy transmission of the long wavelength light through ordered nanopores of the TNTA.[36] The N719-sensitized P-TNTA electrode remains a similar transmittance curve shape, with a considerable light loss in long wavelength region. In contrast, the H-TNTA electrode is opaque (inset of Fig. 5b) with an almost constant transmittance around 9% in the whole wavelength range of 400-800 nm. Most importantly, the transmittance of H-TNTA in the long wavelength region is not as pronounced as that of P-TNTA, due to the light scattering effect of the nanowire cap layer. As a result of scattering, the transmittance of N719-sensitized H-TNTA is decreased more significantly in the long wavelength region (>600 nm) than that in the region of 400-600 nm, as compared with the sensitized P-TNTA.

The photovoltaic performances of DSSCs employing P-TNTA and H-TNTA photoanodes under AM 1.5 front illumination (100 mW cm$^{-2}$) are displayed in Fig. 6a, with the detailed parameters summarized in Table 1. Before comparing the performance of the P-TNTA and H-TNTA based devices, the photovoltaic contribution of the thin adhesive layer (~2 μm) was investigated. The thin TiO$_2$ particle layer contributes a power conversion efficiency of 2.03%, with a short-circuit current density ($J_{sc}$) of 3.12 mA cm$^{-2}$, open-circuit voltage ($V_{oc}$) of 820 mV and fill factor ($FF$) of 0.79. The $J_{sc}$, $V_{oc}$ and $FF$ are 10.97 mA cm$^{-2}$, 751 mV and 0.659 for

the P-TNTA cell, respectively, leading to a power conversion efficiency of 5.43%. As a result of doubled dye loading and strong light scattering, the $J_{sc}$ of the H-TNTA device increases from 10.97 to 16.72 mA cm$^{-2}$, with the $V_{oc}$ and $FF$ almost unchanged, leading to a high efficiency up to 8.21%, ~ 51% higher than that of its counterpart, the P-TNTA based device.
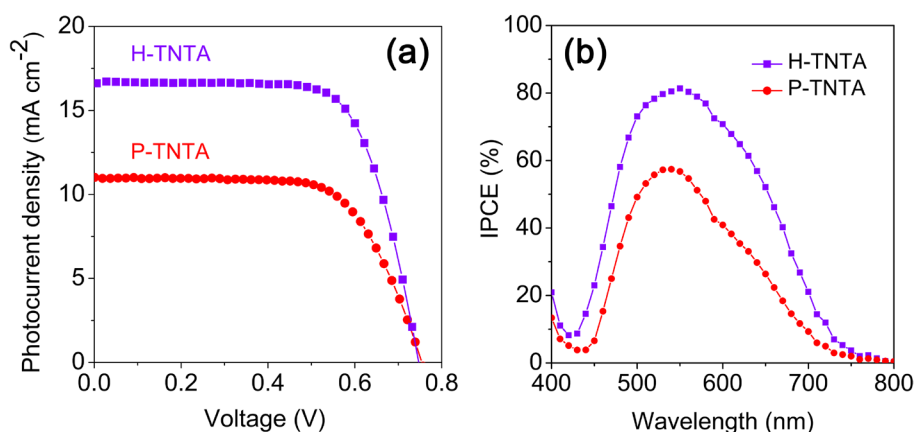


**Fig. 6** (a) Photocurrent-photovoltage characteristics of the DSSCs based on P-TNTA and H-TNTA photoanodes, measured under 1 sun illumination; (b) IPCE spectra of the P-TNTA and H-TNTA based DSSCs.

The incident photo-to-current conversion efficiency (IPCE) spectra were recorded to investigate the $J_{sc}$ and efficiency enhancement of the H-TNTA based DSSCs. As shown in Fig. 6b, the IPCE of the H-TNTA device exhibits a prominent increase in the whole wavelength range of 400-800 nm, which is resulted from the increased dye loading and the enhanced light scattering in the hybrid structure of H-TNTA. It is worth noting that the relative increase in IPCE is more pronounced in long wavelength region (600-800 nm) than that in the 450-600 nm range. For example, the IPCE of H-TNTA is increased by 37% at 550 nm (81.1% vs 58.8%), whereas it is 97% at 650 nm (52.1% vs 26.4%), compared with that of P-TNTA. This is mainly attributed to the light scattering from the nanowire cap layer of the

**Table 1** Photovoltaic parameters of the P-TNTA and H-TNTA based DSSCs.[a]

| Device | Thickness [μm] | BET surface area [m² g⁻¹] | Dye-loading [×10⁻⁷mol cm⁻²] | IPCE [b] [%] | $J_{sc}$ [mA cm⁻²] | $V_{oc}$ [V] | FF | η [%] |
|---|---|---|---|---|---|---|---|---|
| P-TNTA | 22.8 | 24.6 | 1.02 | 58.8 | 10.97 | 0.751 | 0.659 | 5.43 |
| H-TNTA | 24.1 | 46.8 | 2.19 | 81.4 | 16.73 | 0.746 | 0.662 | 8.21 |

[a]Data listed here are the average values over five devices. [b]Values at 550 nm.

H-TNTA electrode, since the increased optical path length due to light-scattering is more effective for light harvesting enhancement in a wavelength range where the N719 dye has a poor absorption. While in short wavelength range where the N719 has a very strong absorption, the scattering effect becomes less effective. According to the equation of $J_{sc} = q\eta_{lh}\,\eta_{inj}\,\eta_{cc}\,I_0$, the remarkable increase of $J_{sc}$ can be mainly attributed to the increase of the light-harvesting efficiency, $\eta_{lh}$, since the charge collection efficiency is similar for P-TNTA and H-TNTA electrodes (will be proved by EIS and IMPS/VS later) and the difference of charge-injection efficiency in this two kinds of devices can be ignored.[42] The integrated $J_{sc}$ ($J_{sc,\,INT}$) from the IPCE results is 15.22 and 9.78 mA cm⁻² for the H-TNTA and P-TNTA based devices, respectively. The deviation of the $J_{sc,\,INT}$ from the measured $J_{sc}$ (by *IV* test) is believed to be resulted from the ionic transport limitation of the electrolyte inside the thick TNTA based photoanodes (~24 μm in thickness in the present study).[43-46] However, the $J_{sc,INT-H-TNTA}/J_{sc,INT-p-TNTA}$ ratio (1.56) is similar to measured $J_{sc-H-TNTA}/J_{sc-p-TNTA}$ ratio (1.53). It can be concluded that the increase in $\eta_{lh}$ for H-TNTA is due to increased dye attachment and enhanced light scattering in the designed hierarchical electrode.

The electrochemical properties of the DSSCs with various photoanodes were investigated by the electrochemical impedance spectroscopy (EIS) carried out under 1 sun (100 mW cm$^{-2}$) illumination. The parameters (Table 2) related to the electron transport and transfer were extracted from the EIS results by fitting the Nyquist plots (Fig. 7) according to the equivalent circuit based on a transmission line model (Fig. 7a). Interestingly, the electron transport resistance, $R_w$, of the H-TNTA is 2.2 Ω which is even smaller than that (2.95 Ω) of the P-TNTA cell, though the H-TNTA tube-wall is thinner and full of nanoparticles. It is believed that the decreased $R_w$ is due to the improved conductivity of the dye-sensitized TiO$_2$
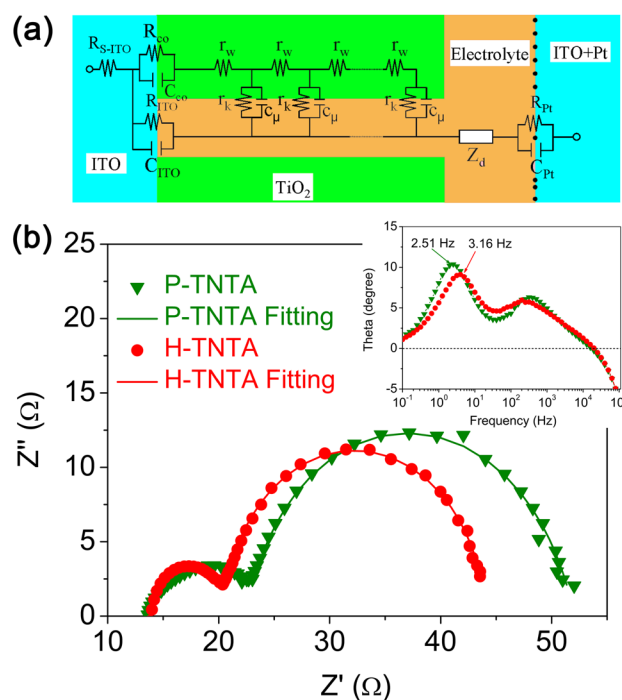


**Fig. 7** (a) The equivalent circuit of the full DSSC represented by a transmission line model. (b) The Nyquist and Bode phase (inset) plots of the P-TNTA and H-TNTA based DSSCs measured under AM 1.5 solar illumination (100 mW cm$^{-2}$).

film under illumination, since the H-TNTA which exhibits a much better light-harvesting efficiency will inject more electrons into the conduction band and hence increase the steady

state electron density and the conductivity of the $TiO_2$. As summarized in Table 2, the electron diffusion coefficient, $D_{eff}$, is $8.09 \times 10^{-4}$ and $12.4 \times 10^{-4}$ $cm^2$ $s^{-1}$ while the electron transport time, $\tau_d$, is 6.43 and 4.70 ms for P-TNTA and H-TNTA, respectively, indicating faster electron transport in the H-TNTA. The charge transfer resistance ($R_k$) at the $TiO_2$/dye/electrolyte interface is 29.1 $\Omega$ for P-TNTA and 23.6 $\Omega$ for H-TNTA, indicating that the electron recombination at the $TiO_2$/dye/electrolyte interface of H-TNTA is slightly faster than that of P-TNTA. The electron life time ($\tau_e$) is 50.4 and 63.4 ms for H-TNTA and P-TNTA, respectively, calculated according to the Bode phase plot (inset of Fig. 7b) and $\tau_e = 1/2\pi f_{max}$, where the $f_{max}$ is the peak frequency corresponding to the second arc in the Nyquist plot. The smaller $R_k$ and $\tau_e$ of H-TNTA arises from its larger specific surface area which offers more trap states for electron recombination, in agreement with the slightly decreased $V_{oc}$, when compared with the P-TNTA cells. According to $\eta_{cc} = 1 - R_w/R_k$, the H-TNTA and P-TNTA devices exhibit similar high charge collection efficiencies of 90.7% and 89.9%, respectively.

Table 2 Parameters extracted from the EIS tests measured under AM 1.5 illumination.

| Device | $R_w$ [$\Omega$] | $R_k$ [$\Omega$] | $\tau_d$ [ms] | $\tau_e$ [ms] | $D_{eff}$ [$cm^2$ $s^{-1}$] | $\eta_{cc}$ [%] |
|--------|------------------|------------------|---------------|---------------|------------------------------|------------------|
| P-TNTA | 2.95 | 29.1 | 6.43 | 63.4 | $8.09 \times 10^{-4}$ | 89.9 |
| H-TNTA | 2.2 | 23.6 | 4.70 | 50.4 | $12.4 \times 10^{-4}$ | 90.7 |

Intensity-modulated photocurrent spectroscopy and photovoltage spectroscopy (IMPS and IMVS) were performed to further investigate the electron transport and recombination behaviors in the DSSCs based on the two photoanodes. The electron transport time ($\tau_d$) and

electron life time ($\tau_e$) which represent the time constant of the injected electrons transporting across the semiconductor film and recombining with $I_3^-$ in the electrolyte, respectively, can be derived from the obtained IMPS and IMVS results according to $\tau_e = 1/2\pi f_{min}$, where $f_{min}$ is the characteristic minimum frequency of the IMPS/IMVS imaginary component. Fig. 8a displays the $\tau_e$ and $\tau_d$ of H-TNTA and P-TNTA devices as a function of the incident photon fluxes. The $\tau_e$ of the H-TNTA is only slightly smaller than P-TNTA, due to the improved surface area of the nanowire-nanoparticle/nanotube architecture. The $\tau_d$ of H-TNTA is shorter than P-TNTA, especially under high light intensity, indicating the faster electron transport in dye-sensitized H-TNTA hierarchical architecture under irradiation. The $\eta_{cc}$ can be estimated according to $\eta_{cc} = 1-(\tau_d/\tau_e)$. Both the H-TNTA and P-TNTA based DSSCs demonstrate a high $\eta_{cc}$ around 95%, as shown in Fig. 8b. The results derived from the IMPS/IMVS measurements are in agreement with that obtained from the EIS and *I-V* tests.
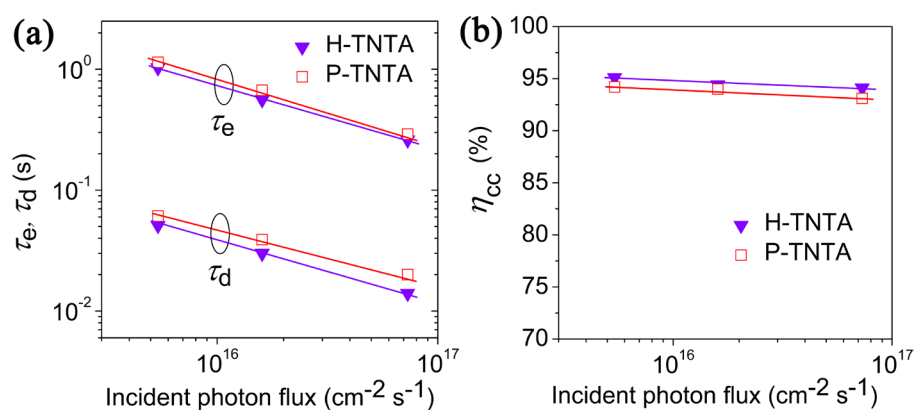


**Fig. 8** (a) Electron life time ($\tau_e$) and transport time ($\tau_d$), and (b) charge collection efficiency ($\eta_{cc}$) of the P-TNTA and H-TNTA based devices as a function of the incident photon fluxes, extracting from the IMVS/IMPS results.

The $TiCl_4$ treatment of the photoanodes is deemed to play a crucial role in improving the specific surface area and the electron transport properties, which will remarkably influence

the photovoltaic performance.[8,9] To this end, the H-TNTA electrodes were subjected to an additional TiCl$_4$ treatment, and the obtained electrodes were employed as photoanodes of DSSCs. As displayed in Fig. 9, both the $J_{sc}$ and $V_{oc}$ of the device were improved after the TiCl$_4$ treatment. An impressive power conversion efficiency as high as 8.82% is achieved with the $J_{sc}$ of 17.68% mA cm$^{-2}$, $V_{oc}$ of 0.754 V, $FF$ of 0.658 and a IPCE of 86.4% at 550 nm.
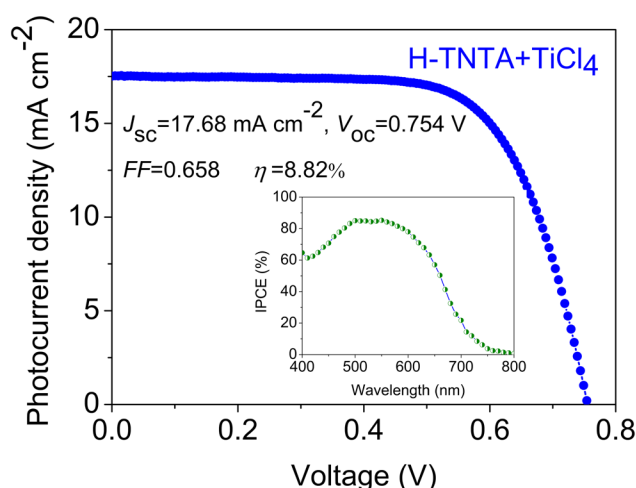


**Fig. 9** *I-V* characteristics of the DSSC based on H-TNTA photoanode with an additional TiCl$_4$ treatment, measured under 100 mW cm$^{-2}$ illumination.

**Conclusion**

In summary, we have successfully proposed a green, simple but effective hot water post-treatment technique to fabricate hierarchical TNTA architecture for efficient DSSCs. The produced impurity free TiO$_2$ nanowire-nanoparticle/nanotube structure demonstrates complementary and synergistic properties, in which the 1D TNTA scaffold provides a vectorial pathway for fast electron transport along the long tube axial direction toward the FTO collection electrode; the small TiO$_2$ nanoparticles decorated on the wall surface provide the photoanode with a large specific surface area for dye attachment; the TiO$_2$ nanowire cap layer offer prominent light-scattering as well as dye-loading. When this well-tailored film was

exploited as the photoanode of a DSSC, a high efficiency up to 8.21% was yielded, 51% higher than that of the DSSC based on pristine TNTA. The efficiency can be further improved to 8.82% by adopting a subsequent $TiCl_4$ treatment. It is believed that the technique proposed here is also promising for QDSSCs and other photoelectrochemical applications.

## Acknowledgement

Reference

1.  A. Yella, H. W. Lee, H. N. Tsao, C. Y. Yi, A. K. Chandiran, M. K. Nazeeruddin, E. W. G. Diau, C. Y. Yeh, S. M. Zakeeruddin and M. Grätzel, *Science*, 2011, **334**, 629-634.

2.  I. Chung, B. Lee, J. Q. He, R. P. H. Chang and M. G. Kanatzidis, *Nature*, 2012, **485**, 486-490.

3.  J. H. Wu, Y. M. Xiao, Q. W. Tang, G. T. Yue, J. M. Lin, M. L. Huang, Y. F. Huang, L. Q. Fan, Z. Lan, S. Yin and T. Sato, *Adv. Mater.*, 2012, **24**, 1884–1888.

4.  H. P. Zhou, Q. Chen, G. Li, S. Luo, T. B. Song, H. S. Duan, Z. R. Hong, J. B. You, Y. S. Liu and Y. Yang, *Science*, 2014, **345**, 542-546.

5.  N. Q. Fu, Y. Y.Fang, Y. D. Duan, X. W. Zhou, X. R. Xiao and Y. Lin, *ACS Nano*, 2012, **6**, 9596-9605

6.  W. Q. Wu, Y. F. Xu, H. S. Rao, C. Y. Su and D. B. Kuang, *J. Am. Chem. Soc.*, 2014, **136**, 6437−6445.

7.  M. D. Ye, X. K. Xin, C. J. Lin and Z. Q. Lin, *Nano Lett.*, 2011, **11**, 3214–3220.

8.  S. So, I. Hwang and P. Schmuki, *Energy Environ. Sci.*, 2015, **8**, 849–854.

9.  J. Choi, G. Kang, and T. Park, *Chem. Mater.*, 2015, **27**, 1359−1366.

10. W. Q. Wu, Y. F. Xu, C. Y. Su and D. B. Kuang, *Energy Environ. Sci.*, 2014, **7**, 644–649.

11. H. P. Wu, C. M. Lan, J. Y. Hu, W. K. Huang, J. W. Shiu, Z. J. Lan, C. M. Tsai, C. H. Su and E. W. G. Diau, *J. Phys. Chem. Lett.*, 2013, **4**, 1570−1577.

12. N. Q. Fu, Y. D. Duan, Y. Y. Fang, X. W. Zhou, X. R. Xiao and Y. Lin, *Electrochem. Commun.*, 2013, **34**, 254–257.

13. Z. H. Dong, X. Y. Lai, J. E. Halpert, N. L. Yang, L. X. Yi, J. Zhai, D. Wang, Z. Y. Tang

and L. Jiang, *Adv. Mater.*, 2012, **24**, 1046–1049.

14. N. Q. Fu, Y. D. Duan, Y. Y. Fang, X. W. Zhou, Y. C. Liu, F. Peng, Y. Lin and H. T. Huang, *J. Power Sources*, 2014, **271**, 8-15.

15. S. Ito, T. N. Murakami, P. Comte, P. Liska, C. Grätzel, M. K. Nazeeruddin and M. Grätzel, *Thin Solid Films*, 2008, **516**, 4613–4619.

16. L. D. Marco, M. Manca, R. Giannuzzi, M. R. Belviso, P. D. Cozzolibc and G. Gigliabc, *Energy Environ. Sci.*, 2013, **6**, 1791–1795.

17. F. Sauvage, D. Chen, P. Comte, F. Z. Huang, L. P. Heiniger, Y. B. Cheng, R. A. Caruso and M. Grätzel, *ACS Nano*, 2010, **4**, 4420–4425.

18. J. T. Zhang, M. He, N. Q. Fu, J. Y. Li and X. Yin, *Nanoscale*, 2014, **6**, 4211–4216.

19. Z. S. Xue, C. Y. Jiang, L. Wang, W. Liu and B. Liu, *J. Phys. Chem. C*, 2014, **118**, 16352−16357.

20. B. Liu and E. S. Aydil, *J. Am. Chem. Soc.*, 2009, **131**, 3985–3990.

21. Q. L. Huang, G. Zhou, L. Fang, L. P. Hua and Z. S. Wang, E*nergy Environ. Sci.*, 2011, **4**, 2145–2151.

22. N. Tétreault, E. Horváth, T. Moehl, J. Brillet, R. Smajda, S. Bungener, N. Cai, P. Wang, M. Zakeeruddin, L. Forró, A. Magrez and M. Grätzel, *ACS Nano*, 2010, **4**, 7644–7650.

23. W. Q. Wu, H. L. Feng, H. S. Rao, Y. F. Xu, D. B. Kuang and C. Y. Su, *Nat. Commun.*, 2014, **5**, 3968 (1-9).

24. W. Q. Wu, B. X. Lei, H. S. Rao, Y. F. Xu, Y. F. Wang, C. Y. Su and D. B. Kuang, *Sci. Rep.*, 2013, **3**, 1352 (1-7).

25. C. T. Yip, H. T. Huang, L. M. Zhou, K. Y. Xie, Y. Wang, T. H. Feng, J. Li and W. Y.

Tam, *Adv. Mater.*, 2011, **23**, 5624–5628.

26. M. Guo, K. Y. Xie, J. Lin, Z. H. Yong, C. T. Yip, L. M. Zhou, Y. Wang and H. T. Huang, *Energy Environ. Sci.*, 2012, **5**, 9881–9888.

27. S. Foster and S. John, *Energy Environ. Sci.*, 2013, **6**, 2972–2983.

28. H. Y. Chen, D. B. Kuang and C. Y. Su, *J. Mater. Chem.*, 2012, **22**, 15475–15489.

29. X. Y. Wang, L. D. Sun, S. Zhang and X. Wang, *ACS Appl. Mater. Interfaces*, 2014, **6**, 1361−1365.

30. X. L. Liu, M. Guo, J. Lin, X. F. Chen and H. T. Huang, *RSC Adv.*, 2014, **4**, 45180–45184.

31. S. Lee, I. J. Park, D. H. Kim, W. M. Seong, D. W. Kim, G. S. Han, J. Y. Kim, H. S. Jung and K. S. Hong, *Energy Environ. Sci.*, 2012, **5**, 7989–7995.

32. D. Kim, A. Ghicov, S. P. Albu and P. Schmuki, *J. Am. Chem. Soc.*, 2008, **130**, 16454–16455.

33. J. Lin, X. L. Liu, M. Guo, W. Lu, G. G. Zhang, L. M. Zhou, X. F. Chen and H. T. Huang, *Nanoscale*, 2012, **4**, 5148–5153.

34. S. Kurian, P. Sudhagar, J. Lee, D. Song, W. Cho, S. Lee, Y. S. Kang and H. Jeon, *J. Mater. Chem. A*, 2013, **1**, 4370–4375.

35. Z. B. Yang, D. Y. Pan, C. Xi, J. H. Li, J. W. Shi, F. Xu, Z. Q. Ma, *J. Power Sources*, 2013, **236**, 10–16.

36. P. Poudel and Q. Qiao, *Nanoscale*, 2012, **4**, 2826–2838.

37. Z. L. He, W. X. Que, P. Sun and J. B. Ren, *ACS Appl. Mater. Interfaces*, 2013, **5**, 12779−12783.

38. F. Z. Huang, D. H. Chen, X. L. Zhang, R. A. Caruso and Y. B. Cheng, *Adv. Funct. Mater.*,

2010, **20**, 1301–1305.

39. L. J. Yang and W. W. F. Leung, *Adv. Mater.* 2011, **23**, 4559–4562.

40. K. Lee, A. Mazare and P. Schmuki, *Chem. Rev.*, 2014, **114**, 9385–9454.

41. N. Fuke, A. Fukui, A. Islam, R. Komiya, R. Yamanaka, L. Y. Han and H. Harima, *J. Appl. Phys.*, 2008, **104**, 064307..

42. Q. Wang, S. Ito, M. Grä1tzel, F. Fabregat-Santiago, I. Mora-Seró, J. Bisquert, T. Bessho and H. Imai, *J. Phys. Chem. B*, 2006, **110***,* 25210-25221.

43. X. Z. Guo, Y. H. Luo, C. H. Li, D. Qin, D. M. Li and Q. B. Meng, *Curr. Appl. Phys.*, 2012, **12**, e54-e58.

44. A. C. Fisher, L. M. Peter, E. A. Ponomarev, A. B. Walker and K. G. U. Wijayantha, *J. Phys. Chem. B.*, 2000, **104**, 949-958.

45. T. Trupke and P. Würfel, *J. Phys. Chem. B.*, 2000, **104**, 11484-11488.

46. V. Shrotriya, G. Li, Y. Yao, T. Moriarty, K. Emery and Y. Yang, *Adv. Func. Mater.*, 2006, **16**, 2016-2023.